Chemical Engineering Journal 527 (2026) 171682

Contents lists available at ScienceDirect

Chemical Engineering Journal

journal homepage: www.elsevier.com/locate/cej

Visible light accelerated CO_2 hydrogenation to CO over a Cu/ZnO/Al_2O_3 catalyst: Teaching an old dog new tricks

Miha Okorn [a,b], Giovanni Cardolini Rizzo [c], Kristijan Lorber [a], Matjaž Mazaj [a], Nataša Novak Tušar [a,b], Petar Djinović [a,b,*]

[a] National Institute of Chemistry, Hajdrihova 19, 1000, Ljubljana, Slovenia
[b] University of Nova Gorica, Vipavska 13, 5000, Nova Gorica, Slovenia
[c] Politecnico di Torino, Corso Duca degli Abruzzi 24, 10129, Torino, Italy

ARTICLE INFO

Keywords:
CO_2 utilization
In-situ spectroscopy
Kinetic analysis
Reaction mechanism
Light-assisted catalysis

ABSTRACT

The Cu-ZnO-Al_2O_3 is a proven catalyst for thermally-driven RWGS reaction. In this work, its ability to function as photo-catalyst in the light-assisted RWGS reaction was analyzed. By utilizing the synergy of visible light and thermal energy, CO formation was accelerated almost 6-times compared to reaction in dark. Wavelength-dependent and kinetic analysis confirmed that blue photons are most efficient for accelerating the CO rate. Differences in the reaction mechanism under dark and illuminated conditions are postulated, based on the drop in apparent activation energy from 83 to 44 kJ/mol and strongly changing reaction orders of H_2 during kinetic analysis. CO formation through the redox reaction mechanism occurs both under dark and illuminated conditions, yet represents only 10 % of the overall CO yield. Transient *in-situ* DRIFTS data showed the decomposition rate of the most abundant surface species (carbonates and formates) is not accelerated by light despite higher catalytic activity, indicating that these abundant surface species are minimally involved in CO formation under illumination. The RWGS reaction under light-assisted conditions proceeds *via* several contributory routes, with the carboxylate mechanism as the main pathway. Light-induced hydrogen dissociation, increased H coverage and its reaction with surface hydroxyls accelerates water formation and desorption after carboxylate decomposition, resulting in accelerated CO rates.

1. Introduction

The CO_2 hydrogenation to CO, also known as the Reverse Water Gas Shift (RWGS) reaction is of particular interest due to the direct use of CO as a feedstock in many important industrial reactions, such as methanol synthesis and the Fischer–Tropsch process, which produces synthetic liquid fuels [1]. RWGS is an endothermic equilibrium reaction ($CO_2 + H_2 \leftrightarrow CO + H_2O$, $\Delta H_r = 50$ kJ/mol), where high CO_2 conversion is enabled at high temperatures. Direct catalytic dissociation of CO_2 is sluggish and energetically demanding, whereas the reaction is greatly accelerated in substantial H_2 excess [2]. Thus, innovative pathways for accelerating the RWGS rate at low temperatures (below 200 °C) and stoichiometric reactant feed are highly desired.

Light-assisted catalysis can be used to influence reaction rates and break the low-temperature equilibrium limitations of the thermally driven catalytic reactions as a result of several phenomena: (i) non-thermal energy input in the form of photons, (ii) modification of binding strength of reactants, intermediates and products, which is induced by altered potential energy landscape of the catalyst in the excited state, and (iii) direct oxidation and reduction of surface species with participation of hot electrons and holes [3]. Light-assisted catalysis can be performed using plasmonic metals (Cu, Au or Ag) which exhibit a strong Localized Surface Plasmon Resonance (LSPR) effect, semiconductors with an appropriate bandgap energy, or preferably both [4,5]. The semiconductor and metal used for the light-assisted catalysis should exhibit intrinsic activity for the catalytic reaction also in the absence of illumination, as reactant adsorption and stabilization of reactive intermediates that lead to the desired product are crucial for catalytic turnover.

Most extensively researched RWGS catalysts are based on Cu, Pt, Pd or Fe nanoparticles, dispersed over different supports, such as Al_2O_3, TiO_2, CeO_2, ZnO, etc. [1,6–8]. Platinum based catalysts are very active, but economically unsuitable due to high price of the noble metal. Also, strong CO binding to the metallic Pt sites overpopulates them, making

* Corresponding author at: National Institute of Chemistry, Hajdrihova 19, 1000, Ljubljana, Slovenia.
E-mail address: petar.djinovic@ki.si (P. Djinović).

https://doi.org/10.1016/j.cej.2025.171682
Received 6 October 2025; Received in revised form 5 December 2025; Accepted 7 December 2025
Available online 13 December 2025

them inaccessible for H_2 activation at low temperatures [9]. Iron based catalysts exhibit good activity and stability at temperatures above 350 °C, whereas copper-based catalysts are widely praised for their good activity in the medium temperature range (200–300 °C) [10].

Yang et al. [11] report that RWGS activity of the 5 % Cu/CeO_2 catalyst increased by 30 % at a catalyst temperature of 250 °C upon visible light illumination. A combination of *in-situ* DRIFTS, EPR, and XPS characterization revealed that under illumination, the LSPR produced by Cu nanoparticles stimulates hot electron transfer to ceria, causing destabilization and desorption of bidentate formate and linearly adsorbed CO. Moreover, the spillover of H_2 from Cu to CeO_2 is also affected by light, leading to regeneration of oxygen vacancies on the CeO_2 surface, which positively influences the CO yield.

Xie and colleagues [12] report that simultaneous excitation of ZnO band-gap (with UV photons) and Cu LSPR (with visible photons) cooperatively promotes methanol-production over the copper/zinc oxide/alumina catalyst. On the other hand, excitation of individual components (Cu or ZnO) leads to the acceleration of the CO rate. The authors report that visible illumination (420–800 nm) causes a change in surface copper oxidation state (enrichment of Cu^{1+} at the expense of Cu^0) and alteration of local electronic structure of ZnO *via* interphase electron migration. At 225 °C and 600 mW/cm^2 irradiance, the CO formation rate was accelerated by about 40 % compared to the reaction in dark.

Zhu and colleagues [13] synthesized a Cu-CeO_2-$SrTiO_{3-\delta}$ heterojunction catalyst. The CO productivity of this catalyst was about 25 % higher under photo-thermal conditions compared to reaction in dark at the same catalyst temperature of 350 °C. The enhanced activity was attributed to the synergistic effect between three catalytic phases: Cu nanoparticles, CeO_2, and $SrTiO_{3-\delta}$, as well as their interfaces. The increase in oxygen vacancy abundance in the CeO_{2-x} phase enhances the adsorption of CO_2, whereas presence of Cu broadens the light absorption range. A significant role is played by the LSPR effect of Cu nanoparticles in promoting the catalytic performance of RWGS.

The Cu-ZnO-Al_2O_3 (CZA) catalyst is an established catalyst for the low-temperature WGS reaction and has been through decades of research optimized in terms of catalytic performance through chemical composition, structural properties, active site abundance and cost of manufacture. In addition to catalytic performance under thermally driven conditions, it contains a substantial fraction of copper, which exhibits inter and intra band absorbance, as well as LSPR absorption maximum in the visible range of light spectrum (550–600 nm). As such, it efficiently absorbs visible light which is a prerequisite for light-assisted catalytic performance. Taking a highly performing off-the-shelf catalyst and analyzing its light-assisted catalytic RWGS performance was the aim of this work, instead of *de novo* design and synthesis of photocatalytic material. This work is focused on investigating the effects of visible light, wavelength and irradiance on the light-driven rate of CO formation using a CZA catalyst. *In-situ* spectroscopy, transient isothermal experiments and kinetic analysis were applied to reveal mechanistic differences between the RWGS reaction under dark and illuminated conditions and identify the reasons for accelerated CO formation rate under illumination.

2. Experimental section

2.1. Characterization methods

A Cu-ZnO-Al_2O_3 catalyst, noted as CZA in the manuscript was purchased from Alfa Aesar (product number 045468, LOT: E06T063; Cu: 35.8 wt% (44.8 wt% CuO); Zn: 21 wt% (26.2 wt% ZnO); Al: 7.5 wt% (14.2 wt% Al_2O_3); 15 wt% graphite as binder). BET specific surface area, BJH total pore volume, pore size distribution and the average pore size were determined from the N_2 adsorption/desorption isotherm measured at −196 °C (Micromeritics, model TriStar II 3020). The sample was degassed prior to analysis (SmartPrep degasser, Micromeritics) in N_2 flow for 16 h at 300 °C.

FE-SEM SUPRA 35VP (Carl Zeiss) field-emission scanning electron microscope was used to visualize the surface morphology and spatially analyze the elemental distribution using EDXS.

The *in-situ* Vis DR spectroscopy was performed on a Lambda 650 spectrometer (Perkin Elmer) using the reaction chamber from Harrick (model HVC-VUV-5). Finely powdered sample (10 mg) was analyzed after *in-situ* activation in a 5 % H_2/N_2 flow at 320 °C for 30 min, followed by cooling to 230 °C. Spectralon® was used to record the background.

X-ray diffraction analysis was performed to identify the crystalline phases in the activated CZA catalyst. Prior to analysis, the sample was *ex-situ* activated in 5 % H_2/Ar flow at 320 °C for 30 min. After cooling to room temperature in 5 % H_2/Ar flow, the sample was carefully transferred to the apparatus and analyzed.

In-situ X-ray diffraction analysis was performed to quantify and compare the crystalline phases present in the CZA catalyst after activation and during the dark and light-assisted RWGS conditions. Experiments were performed using Malvern Empyrean diffractometer (2θ range between 20 and 80°, step of 0.039°) under dark and illuminated RWGS conditions after sample activation (30 min at 320 °C in 10 % H_2/N_2 flow, followed by cooling to 230 °C) and exposure to equimolar H_2/CO_2 flow (20 ml/min) inside the Harrick reaction chamber. Reaction chamber was covered with a Kapton® foil and illuminated by Schott KL2500 LED source (9 mm I.D. optic fiber, white light, 550 mW/cm^2). Quantitative phase analysis was performed from Le Bail fit using Topas Academic v.6 software package. The crystallite sizes of Cu and ZnO were determined using Scherrer equation, based on profile fitting of the most intense diffraction peaks corresponding to the (111) reflection for Cu and the (011) reflection for ZnO.

The H_2 pulse chemisorption and H_2-TPD experiments were performed using 22 mg of CZA sample which was positioned inside the Harrick reaction chamber and activated in 10 % H_2/Ar flow (20 ml/min) for 30 min at 320 °C. Afterwards, the flow was switched to argon (20 ml/min) and the sample was flushed for about 80 min; until the $m/z = 2$ fragment (followed by mass spectrometer, model DSMS from Hiden analytical) dropped to a constant value. The sample temperature was lowered to 170 °C and ten pulses of 10 % H_2/Ar (pulse volume was 250 μl, introduced by a manually operated 6-port valve by Vici) were injected over the sample. After chemisorption, H_2-TPD was initiated by heating the sample to 350 °C. After desorption, the sample was illuminated by 790 mW/cm^2 of white light (LED source Schott KL2500) and the sample temperature was lowered to 170 °C. Ten pulses of 10 % H_2/Ar were injected over the sample, followed by H_2-TPD. The H_2 signal areas during pulse chemisorption and desorption were quantified using an external standard and integrated in Origin8 software.

Temperature programmed reduction (TPR) was performed on a Micromeritics AutoChem II 2920 apparatus. 74 mg of a catalyst sample was pretreated at 350 °C in 10 % O_2/N_2 for 30 min. Flow was changed to argon and the sample was cooled to −10 °C. H_2-TPR analysis was performed in a 50 ml/min 5 % H_2/Ar flow. The samples were heated from −10 to 320 °C with a 5 °C/min ramp. A liquid nitrogen–isopropyl alcohol cold trap was used to remove water vapor before entering the TCD detector.

The N_2O chemisorption was used for the calculation of copper dispersion and Cu average size. After reduction (5 % H_2/N_2 flow at 320 °C for 30 min), the sample was degassed in argon flow at 330 °C and cooled to 35 °C for N_2O chemisorption. To selectively probe only metallic copper surface sites and avoid titration of oxygen vacancies of CeO_2, N_2O pulsing (0.5312 ml pulses containing 10 % N_2O in helium) was performed at 35 °C. Decomposition of N_2O and formation of N_2 were monitored using a mass spectrometer (model DSMS from Hiden analytical, ion fragments $m/z = 28$, 32 and 44 were monitored for N_2, O_2 and N_2O, respectively).

The *in-situ* DRIFTS analysis was performed using a Frontier spectrometer (Perkin Elmer) equipped with a MCT detector. Spectra were collected between 800 and 4000 cm^{-1}, averaged over 16 accumulations with spectral resolution of 4 cm^{-1}. The powdered sample was activated

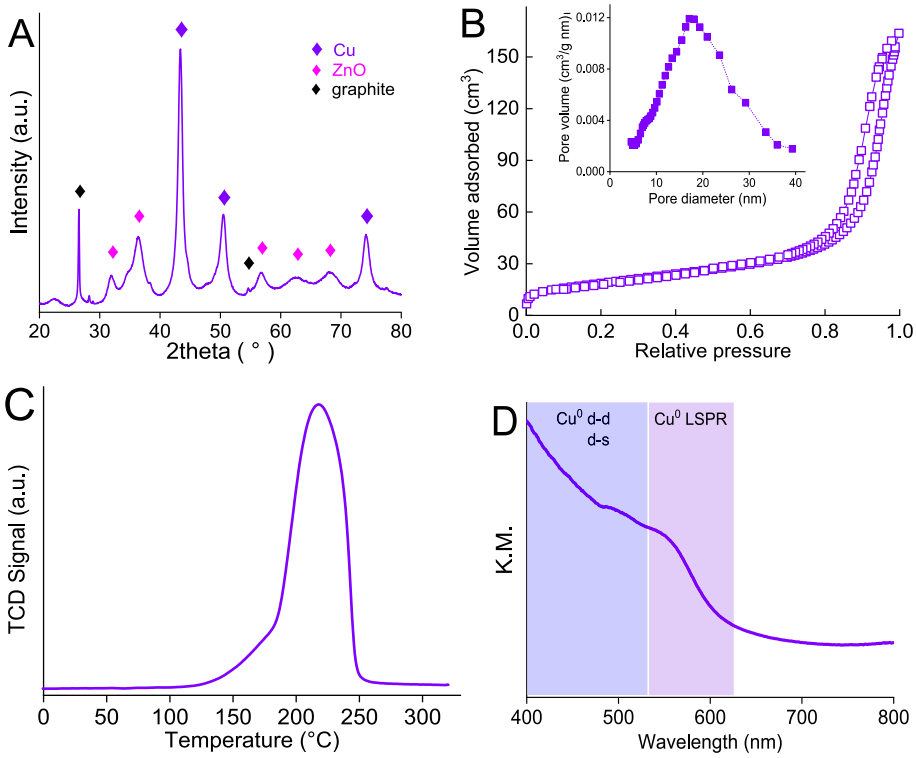

Fig. 1. A) X-ray diffraction pattern of the activated CZA catalyst, B) N_2 sorption isotherm (inset shows pore size distribution), C) H_2-TPR profile of the CZA catalyst and D) Vis-DR spectrum of the activated CZA catalyst, recorded at 230 °C in 5 % H_2/N_2 flow.

in-situ (5 % H_2/N_2 flow for 30 min at 320 °C) and cooled to 230 °C. At this point, background spectrum was recorded and flow was changed to 50 % H_2 and 50 % CO_2 (40 ml/min total flow). After achieving steady state (no further spectral changes), a manually operated 4-way valve by Vici was used to exchange the CO_2 flow (20 ml/min) with argon (20 ml/min). Spectra were collected continuously using the Timebase© software with a time resolution of 17 s. The light-assisted experiment was performed exactly as described above for the thermocatalytic one, except that the sample was irradiated by 250 mW/cm^2 of white light using the Schott KL2500 LED source and the optic fiber.

Transient step change experiments were performed to analyze the effect of water vapor on the RWGS behavior under dark and illuminated conditions was evaluated. The CZA sample (22 mg) was first reduced in 10 % H_2/Ar flow at 320 °C for 30 min, followed by cooling to 230 °C and switching to a 3 % H_2/3 % CO_2/Ar flow (30 ml/min). After reaching a steady output (the following fragments were monitored: $m/z = 2$ (H_2), $m/z = 18$ (H_2O), $m/z = 28$ (CO) and $m/z = 44$ (CO_2) by MS, model DSMS by Hiden analytical), a manually operated 4-way valve by DK-Lok was used to substitute the dry 10 ml/min argon flow with a wet (3 % water vapor/Ar flow of 10 ml/min. Water vapor saturation was achieved by argon passing through a water bubbler that was kept isothermal at 23 °C. After about 45 min exposure to wet RWGS conditions, the switch back to dry argon was made. In all light-assisted experiments, the catalyst was illuminated by 790 mW/cm^2 of white light.

2.2. Catalytic experiments

Catalytic tests were performed in a reaction chamber (Harrick, HVC-MRA-5) which is described in S1 and our previous work [14]. Prior to experiments, absence of mass transfer limitations was verified, see ESI. For all tests, 22 mg of powdered catalyst was used, which formed a round layer with 4.5 mm diameter and 0.5 mm thickness. The catalyst was positioned on a 1 mm thick layer of powdered *SiC* (SiCat, 30–150 μm) to improve heat transfer from the heating element to the sample and minimize the radial temperature gradient inside the catalyst layer. The catalyst temperature was measured with a 0.25 mm K-type thermocouple which was located 0.3 mm below the surface of the catalytic layer. Before the reaction, sample was activated *in-situ* in a 10 ml/min flow of 5 % H_2/N_2 at 320 °C for 30 min. Catalytic experiments were performed between 200 and 320 °C using a 30 ml/min flow containing 50 % H_2 and 50 % CO_2. During the light-assisted RWGS tests, the catalyst was illuminated by a Schott KL2500 LED source (400 nm $< \lambda <$ 700 nm, Fig. S1C), equipped with optic fiber with a 9 mm active diameter. Constant irradiance of 790 mW/cm^2 was used, measured by Thorlabs PM100D photometer. For the wavelength-dependent experiments, Fianium SuperK supercontinuum laser was used to illuminate the samples with 12.7 W/cm^2 irradiance. Gas analysis was performed by GC (model 490 by Agilent, MS5A and PPU columns).

3. Results and discussion

3.1. Structural and chemical analysis

XRD phase analysis of the activated CZA catalyst confirmed the presence of metallic copper crystals, which on average measured 11 nm, Fig. 1A. Metallic copper phase coexists with ZnO, which has an average crystal size of 8 nm. Graphite was also identified in the catalyst, consistent with its role as a lubricant and binder which improves the mechanical strength of the technical catalyst pellet [15]. Alumina could not be identified using diffraction due to its poor crystallinity, however, aluminum presence was confirmed with ICP-OES elemental analysis, see experimental section.

The N_2 adsorption/desorption isotherm of the CZA sample is Type III according to IUPAC classification, characteristic for mesoporous materials containing interparticle porosity, Fig. 1B. The calculated BET specific area was 67 m^2/g, total pore volume equaled 0.25 cm^3/g and the average pore size measured 17 nm.

During the H_2-TPR analysis (Fig. 1C), reduction of the sample occurred between 100 and 280 °C as a single reduction peak with a strong shoulder on the low-temperature side. By taking into

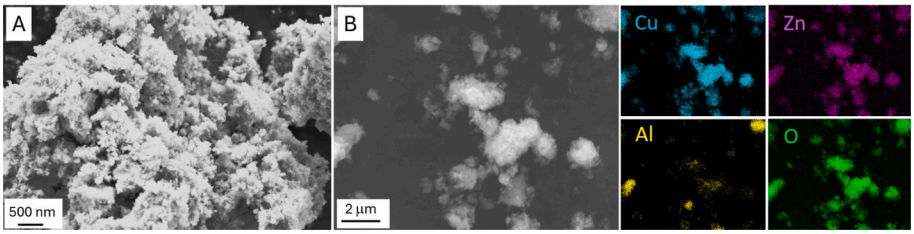

Fig. 2. A) SEM micrograph and B) smaller magnification image with elemental mapping of the CZA catalyst.

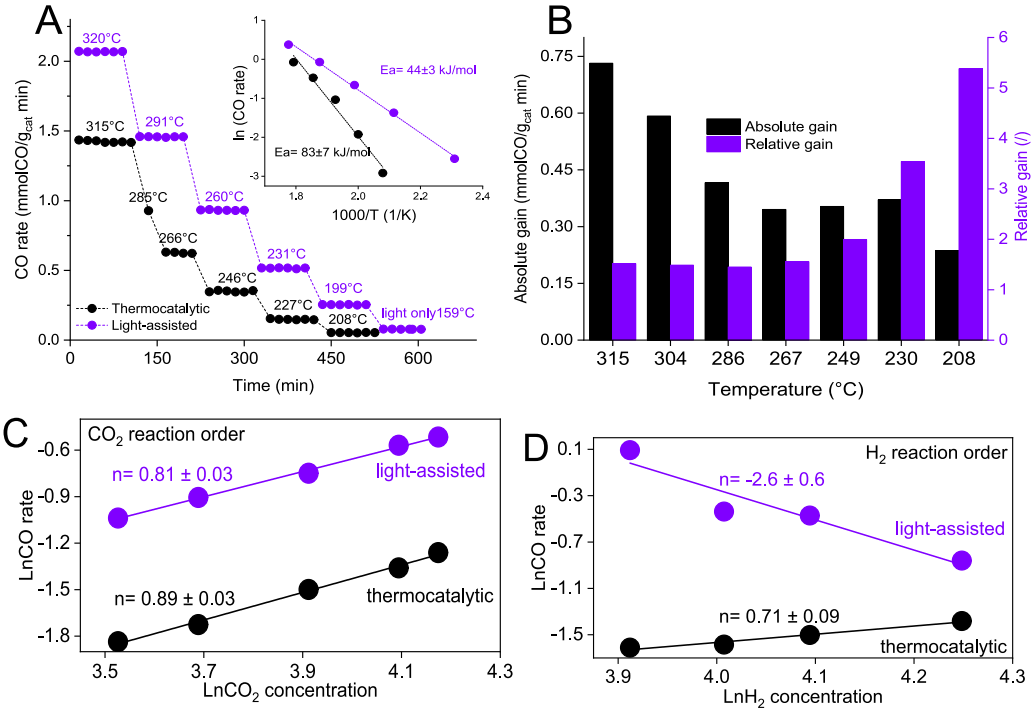

Fig. 3. A) CO rate during thermo-catalytic and light-assisted RWGS reaction at different catalyst temperatures. Inset shows Arrhenius plots for CO formation and corresponding Ea values, B) Relative and absolute CO gains at different catalyst temperatures. C) CO_2 reaction orders during thermocatalytic and light-assisted reaction. D) H_2 reaction orders during thermocatalytic and light-assisted reaction. For kinetic analysis (Fig. 3C and D), the catalyst temperature was maintained constant at 230 °C and a constant white light irradiance of 790 mW/cm^2 was used.

consideration the 129.5 cm^3 H_2/g_{cat} consumed during the analysis, sample mass (74 mg) and copper content of 35.8 wt%, we calculated that all copper was reduced to metallic state ($CuO + H_2 \rightarrow Cu + H_2O$) and 5 % of ZnO was transformed to metallic Zn, where it readily forms the CuZn brass phase [16,17]. The small amount of the formed CuZn phase and overlap of Cu and CuZn diffraction lines prevents its reliable identification from the XRD data. This is consistent with previous analyses that applied *in-situ* XAS for copper and zinc oxidation state quantification during reduction [16,17].

The Vis DR spectrum of the activated CZA sample (Fig. 1D) shows absorption from 400 to 520 nm, originating from inter (d-s) and intra (d-d) band transitions of metallic copper [18]. Brass phase (bimetallic CuZn alloy which is formed during CZA activation) [16,17] has broad interband absorption also in the 400–500 nm region and has no other sharp diagnostic bands. Cu LSPR shows maximum absorption at 559 nm [19]. The LSPR band is weak, which is a collective consequence of small size of copper (11 nm, not optimal for LSPR generation). Also, CuZn alloying, damping from interband transitions or direct contact of individual Cu crystals will diminish the LSPR peak intensity. For nanoparticles below 10 nm, quantum confinement and surface damping strongly quench the LSPR. Strongest and most distinct LSPR typically occurs in this size range of Cu nanoparticles measuring between 30 and 60 nm and shows a well-defined LSPR peak around 560–580 nm [20,21]. Alumina is featureless in the 400–800 nm range and contributes to scattering. ZnO band-edge absorption is expected between ~365–390 nm. Since excitation with UV wavelengths, which could excite ZnO was not possible during light-assisted catalytic experiments (Fig. S1C), this part of the spectrum is not shown in Fig. 1D.

Pulse N_2O chemisorption was used to derive the 8.2 % copper dispersion, which equals an average spherical copper particle diameter of 13.4 nm (see Supporting information). This value is in particularly good agreement with the average copper crystal size (11 nm) estimated from XRD.

SEM visualization showed that CZA catalyst is comprised of flake-like nanoparticles, Fig. 2A. The smaller magnification image was used for EDX mapping (Fig. 2B), which showed that copper, zinc (and oxygen) are homogeneously dispersed, resulting in abundant contact points and interphase between Cu and ZnO. Aluminum distribution was less homogeneous, with clearly distinguishable Al-rich zones.

3.2. *Catalytic performance*

The activity of the CZA catalyst was initially evaluated under H_2-rich (H_2:CO_2 = 2.4:1), CO_2-rich (H_2:CO_2 = 1:1.5) and equimolar H_2/CO_2 feed ratios (Fig. S2). The highest CO rates were observed with equimolar H_2/CO_2 feed, both under dark (thermocatalytic) and light-assisted reaction.

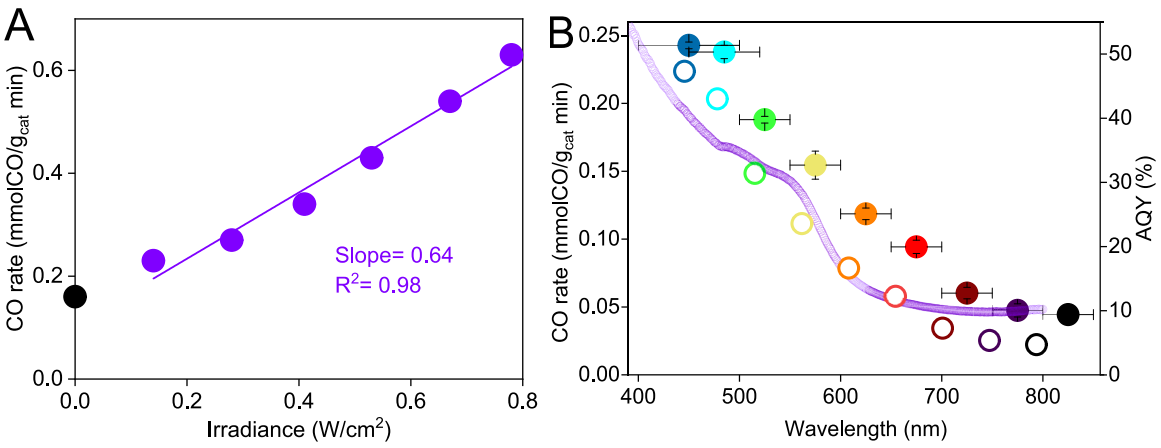

Fig. 4. A) CO rate dependence on irradiance. Black symbol shows CO rate in dark. B) CO rate under illumination with different wavelength ranges at a constant irradiance of 12.7 W/cm^2 (full circles). Empty circles represent apparent quantum yield values. Purple trace shows optical absorption of the activated CZA sample. In both experiments the catalyst temperature was maintained at 230 °C.

Consequently, all subsequent catalytic experiments were conducted using equimolar H_2/CO_2 ratio. Next, the temperature dependence on CO rate was investigated. In dark, the CO formation rate increased exponentially with rising temperature (Fig. 3A) and reached 1.4 mmolCO/(g_{cat} min) at 315 °C. The lowest reaction temperature where CO formed was 208 °C. No methanol was identified under experimental conditions, which is in line with thermodynamic predictions, Fig. S3. The Arrhenius plot analysis (black symbols, inset Fig. 3A) revealed the apparent activation energy (Ea) for CO formation is 83 k/mol, which is in very good agreement with previously reported value (87 k/mol) [22].

The light-assisted RWGS experiment (purple symbols in Fig. 3A) was performed by constantly illuminating the catalyst with 790 mW/cm^2 of visible light and changing the power output of the electric heater to control the catalyst temperature. Catalyst temperature, measured inside the catalytic layer with a miniature thermocouple was used to scale the temperature (Fig. S1). Before the light-assisted experiments, the catalyst was maintained at 320 °C under illumination and kept at this temperature until it reached steady-state activity (Fig. S4A), to ensure catalytic stability.

Similarly to the experiment in dark, CO was the only reaction product. The photocatalytic RWGS reaction was initiated 50 °C earlier compared to experiment in dark: 0.078 mmolCO/(g_{cat} min) was produced already at 159 °C. Under these conditions, no external electric heating was applied and CO formation was driven solely by light irradiation and light-induced sample heating. The Ea in the light-assisted RWGS reaction was 44 kJ/mol (inset Fig. 3A), which is almost halved compared to the value in dark. Such a notably lower Ea value suggests an important, light-induced modification of the reaction mechanism, which enables the CO formation to proceed with a much lower energy barrier.

Next, we compared the absolute and relative CO rate gains between the light-assisted and thermally-driven reactions at identical catalyst temperatures to better quantify the effect of light, Fig. 3B. We defined the absolute rate gain as CO rate difference between the light-assisted rate and the thermally driven rate at identical catalyst temperatures: r(CO) light - r(CO) dark. The absolute CO gain of 0.73 mmolCO/(g_{cat} min) slowly decreased to 0.23 mmolCO/(g_{cat} min) as the catalyst temperature decreased from 315 to 208 °C. The relative CO rate gain is defined as: r(CO) light/r(CO) dark, again, compared at identical catalyst temperature. The light-assisted CO rate was more than five times higher compared to the CO rate under dark conditions at 208 °C. With increasing catalyst temperature, the relative CO gain decreased exponentially, but never dropped below one, revealing the light-assisted RWGS always outperforms the reaction in dark at identical catalyst temperatures. The origin of the decaying photocatalytic contribution with increasing temperature can have multiple origins: The thermally driven reaction channel exhibits exponential (Arrhenius-type) temperature dependence whereas the light-driven reaction channel depends on the number of photons, which was in this experiment constant. Also, inter and intraband electronic transitions quench faster at higher temperatures and intensity of Cu localized surface plasmon resonance (LSPR) decreases with increasing temperature. This behavior is due to several factors: i) At higher temperatures, the density of phonons (vibrational energy in the lattice) increases, leading to greater electron-phonon scattering. This reduces the coherence of the oscillating conduction electrons responsible for the LSPR and broadens the resonance peak, thereby reducing its intensity. ii) Higher temperatures increase energy dissipation mechanisms (such as phonon and defect scattering), further dampening the LSPR. The stability of the CZA catalyst was evaluated at 230 °C under both dark and light-assisted conditions (Fig. S4B). In both cases, the catalytic activity minimally decreased in the first few hours and then reached steady-state, suggesting the light does not affect the long-term stability of the catalyst.

3.3. Kinetic analysis

The identification of CO_2 and H_2 reaction orders was aimed at gaining insight into how visible light irradiation affects the reaction mechanism. The CO synthesis rate r(CO) is expressed by Eq. (1), where k represents the reaction rate constant, c represents the concentration of gas, a and b represent the reaction orders of CO_2 and H_2, respectively.

$$r(CO) = k*c(CO_2)^a*(H_2)^b \quad (1)$$

The Langmuir-Hinshelwood type reaction mechanism is realistically proposed (both reactants chemisorbed on the catalyst surface), since our control experiments identified a minor role of the redox reaction mechanism (Mars-van Krevelen type) both under dark and light-assisted conditions, Fig. S5. Fig. 3C illustrates the relationship between the CO rate and CO_2 concentration (pressure) under dark and light-assisted conditions, while maintaining a constant H_2 concentration. The reaction order with respect to CO_2 remains almost unchanged: 0.89 and 0.81, respectively. The values close to unity suggest that the rate of the RWGS reaction is restricted by dissociation of CO_2 to a similar extent, both under dark and light-assisted conditions [23]. However, upon white light illumination, the H_2 order changes drastically, from +0.7 to −2.6 (Fig. 3D). The strongly negative H_2 reaction order reveals increased surface hydrogen coverage and overcrowding, which is a consequence of the LSPR excitation of Cu, which accelerates H_2 dissociation through hot-carrier injection into H_2 antibonding orbitals and altered surface charge distribution [24].

Using H_2 pulse chemisorption, followed by H_2-TPD under dark and

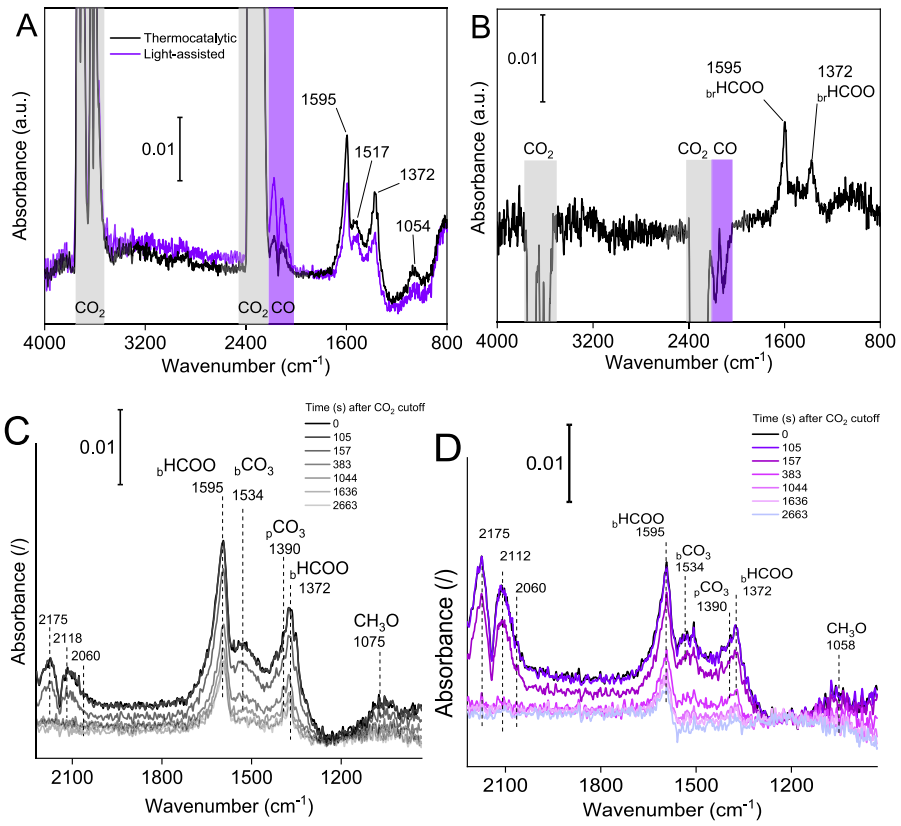

Fig. 5. A) *In-situ* DRIFT spectra during steady-state thermocatalytic and light-assisted RWGS reaction and B) Difference spectrum between thermocatalytic and light-assisted RWGS conditions. Time-resolved DRIFT spectra of the CZA catalyst after the $CO_2 + H_2 \rightarrow H_2 + Ar$ switch under C) thermocatalytic and D) light-assisted reaction conditions where sample was irradiated by 250 mW/cm^2 of white light. Both experiments were performed at a constant catalyst temperature of 230 °C.

illuminated conditions (Fig. S6) we quantified and compared the amounts of chemisorbed hydrogen. The illuminated CZA catalyst chemisorbed $1.5{\cdot}10^{-4}$ mol H_2/g_{cat}, whereas for the CZA catalyst in dark, the amount was about 5 times lower: $2.9{\cdot}10^{-5}$ mol H_2/g_{cat}. The H_2-TPD data directly confirms increased hydrogen coverage under illumination, which is in line with the H_2 reaction orders changing during light-assisted CO_2 methanation over Rh/TiO_2 catalysts [25].

3.4. Irradiance and wavelength effects

The effect of irradiance on the CO rate was investigated at the constant catalyst temperature of 230 °C, Fig. 4A. To maintain the catalyst temperature constant during increasing white light illumination, the output of the electric heater was decreased simultaneously.

The CO rate scaled linearly with increasing irradiance, Fig. 4A. This provides compelling evidence that photon-induced chemical transformations on the catalyst surface, and not thermal effects (*i.e.* local heating of the nanoparticles because of illumination) are responsible for the CO rate acceleration. The linear dependence of photocatalytic rate on irradiance is characteristic of electron-driven chemical transformations on metal surfaces, whereas exponential dependence (Arrhenius type) is characteristic for thermally driven reactions [26,27]. Illumination of the catalyst (at 230 °C) by 790 mW/cm^2 accelerated the CO rate by 346 % compared to the experiment in dark at identical catalyst temperature (0.52 and 0.15 mmolCO/(g_{cat} min), respectively).

To identify the most efficient wavelength for accelerating the RWGS reaction, a range of wavelengths between 400 and 840 nm was tested, Fig. 4B. Only minor CO rate acceleration was achieved by irradiation with NIR photons (between 750 and 840 nm). By progressively transitioning to higher energy photons, the CO rate increased steadily. The most pronounced CO rate acceleration was observed during illumination with wavelengths between 400 and 500 nm, which correlates with the highest light absorption of the catalyst and specifically, the range of inter and intra-band excitations of copper and CuZn alloy [18]. In line with progressively higher CO rates, the calculated apparent quantum yield values (AQY, empty circles in Fig. 4B, Table S1) steadily increased from 4.7 to 47 %. The outstandingly high AQY values compared to other catalyst formulations reported in the literature (Table S2) indicate that the CZA catalyst is very efficient in utilizing blue photons to drive the RWGS reaction. This is related to the optimized chemical composition and structure of the catalyst, resulting in a large abundance of catalytically active sites that also perform the light absorbing function where the hot carriers have a high probability to induce a catalytic turnover.

3.5. Analysis of reaction channels

The RWGS reaction under thermocatalytic conditions was previously suggested to proceed through redox, carboxylate or formate pathways, which are still debated. Lately, however, both theoretical and experimental evidence suggests the carboxylate as the dominant reaction pathway [28–32]. The ongoing differences in opinion can be traced to diverse reaction conditions (temperature and feed composition) and a multitude of chemically active and inert supports, as well as active metals. On the other hand, very scarce information on RWGS reaction mechanisms under light-assisted conditions with copper-based catalysts exists [12,21].

We first probed the existence of the redox mechanism under thermocatalytic and light-assisted conditions, which was proposed initially as the main route to CO over copper-based catalysts [23,33]. During the redox mechanism, metallic copper switches its oxidation state to Cu^{2+}, which is caused by oxidation with CO_2 and formation of CO molecule ($Cu + CO_2 \rightarrow CuO + CO$). The catalytic cycle is closed by reduction of the CuO phase with H_2, which regenerates the metallic Cu site and produces a water molecule ($CuO + H_2 \rightarrow Cu + H_2O$).

Table 1
Decay rates for different surface species under thermocatalytic (T) and light-assisted (L) reaction conditions, together with the relative L/T ratio.

Peak assignation and position, cm^{-1}	Decay rate (T), s^{-1}	Decay rate (L), s^{-1}	L/T
$_bHCOO + {}_pCO_3$, 1372	3.4 ± 0.2	1.9 ± 0.5	0.6 ± 0.3
$_bCO_3$, 1534	1.8 ± 0.5	2.2 ± 0.4	1.2 ± 0.5
$_bHCOO$, 1595	4.1 ± 0.3	4 ± 0.3	1 ± 0.1

CO produced through the redox mechanism in dark (CO_2 pulsing over the reduced and degassed CZA catalyst in helium flow at 230 °C) represented 10 % of all CO when compared to CO formed during CO_2 pulsing over the CZA catalyst in 5 % H_2/Ar flow (RWGS reaction occurring through all active reaction channels, Fig. S5 and Supporting information). The relative contribution of the redox mechanism to CO formation during the light-assisted experiment was also 10 %, yet the total amount of CO formed was 35 % higher under illumination, revealing a notable effect of light on this reaction channel.

We further analyzed the reactivity of most abundant surface species under dark and light-assisted RWGS using *in-situ* DRIFT spectroscopy at 230 °C. During steady-state conditions (Fig. 5A), characteristic bands of gas phase CO_2 (bands between 2200 and 2400 and combination bands between 3500 and 3750 cm^{-1}) and gas phase CO (2112 cm^{-1} and 2175 cm^{-1}) were observed. The latter support the occurrence of the RWGS reaction. In addition, bidentate formate ($_bHCOO$ 1595 cm^{-1} and 1372 cm^{-1}), bidentate and polydentate carbonates ($_bCO_3$ 1534 cm^{-1} and $_pCO_3$ 1390 cm^{-1}) and methoxy species (CH_3O 1058 cm^{-1}) were observed [28,34–36]. Negligible signal in the C—H vibrational range of 2800–3000 cm^{-1}, expected from formate and methoxy species was observed. The C—H signal is much weaker compared to C═O signal due to a combination of factors like bond polarity and the change in dipole moment during vibration: the C═O bond's significant change in dipole moment during stretching leads to a much stronger IR absorption and intensity [37].

The steady-state difference spectrum (dark DRIFT spectrum minus the light-assisted DRIFT spectrum, Fig. 5B) revealed that bridging formate species ($_bHCOO$) are more abundant in dark, together with less gaseous CO produced, revealing lower RWGS activity in dark which is consistent with catalytic data in Figs. 3A and 4A.

After achieving steady-state surface population, a step-change switch was introduced where carbon dioxide was replaced by argon ($CO_2 + H_2 \rightarrow H_2 + Ar$), Fig. 5C and D. After the switch, the intensity of all surface species progressively decreased. This indicates that all surface species on the catalyst are either reacting with hydrogen or desorbing, resulting in progressive cleaning of the catalysts' surface. After 2663 s in 5 % H_2/Ar flow at 230 °C, only weak signals at 1595, 1390 and 1372 cm^{-1}, belonging to bidentate formate and polydentate carbonate could be observed on the dark CZA, Fig. 5C. The extent of surface cleaning was more extensive on the illuminated CZA as only a weak band at 1595 cm^{-1}, attributed to bidentate formate was remaining 2663 s after the switch, Fig. 5D.

The initial signal decay rates of the most abundant surface species were further compared to analyze which species are most influenced by light, Table 1 and Fig. S7A. Since reactivity of surface species depends also on their coverage, [38] the signal decay rates in the initial 140 s after the switch were compared, as they best mimic the quasi steady-state behavior.

The band at 1372 cm^{-1} is jointly contributed by bidentate formate ($_bHCOO$) and polydentate carbonate ($_pCO_3$), the band at 1534 cm^{-1} is attributed to bidentate carbonate ($_bCO_3$) and the band at 1595 cm^{-1} belongs to bidentate formate ($_bHCOO$), Table 1. Other bands were too small to enable reliable analysis and were thus omitted.

Under thermocatalytic conditions, the signal of $_bHCOO$ at 1595 cm^{-1} decays about two-fold faster compared to $_bCO_3$ at 1534 cm^{-1} (decay rates of 4.1 and 1.8, respectively). The decay rate of the combined $_bHCOO + {}_pCO_3$, band at 1372 cm^{-1} is slower compared to $_bHCOO$ band at 1595 cm^{-1} (3.4 compared to 4.1, respectively). This can be rationalized with the fact that polydentate carbonate ($_pCO_3$) was previously identified by Lorber as considerably more stable compared to bidentate carbonate and formate species [34,36].

Under the light-assisted conditions, the decay rates of $_bHCOO$ at 1595 cm^{-1} and $_bCO_3$ at 1534 cm^{-1} were very similar to the ones in dark. This is manifested also through the L/T ratios: 1 and 1.2, respectively. However, the combined $_bHCOO + {}_pCO_3$ band decayed notably slower under illumination, compared to dark ($L/T = 0.6$). The combined 1372 cm^{-1} band under illumination is contributed mainly by $_pCO_3$, since the steady-state difference spectra showed lesser formate coverage, Fig. 5B. As demonstrated by time-resolved DRIFTS, the reactivity of carbonates and formates was not promoted by illumination, meaning their contribution to enhanced photocatalytic CO rate is not significant. Zhang and colleagues [39] used DFT to analyze the reactivity of formates on Cu [111] and Cu-Cu_2O interface in dark. Rather than decomposition, accumulation of formate spectators was predicted, preventing any catalytic activity at temperatures below 200 °C. Microkinetic analysis of surface species coverage revealed that bidentate formate and atomic H are the most abundant surface intermediates on copper (111) with fractional coverage in the range between 0.1 and 0.4. Coverage of all other species is at least two orders of magnitude lower [40]. These microkinetic and DFT predictions are in line with our *in-situ* DRIFTS results (Fig. 5) where formates dominated the IR spectra of the working catalyst, and our H_2-TPD results as illumination increased hydrogen coverage fivefold on the CZA surface, Fig. S6 [41].

Gas phase CO_2 signal decays quickly (in about 75 s, Fig. S7A) below detection limit and its transient response is independent of illumination (decay rates are comparable within the margin of measurement error).

The decay rate of the gas phase CO signal is initially three-fold faster upon illumination compared to the experiment in dark. After about 80s after the switch, the CO decay rate abruptly changes and becomes equal to the one of the experiment in the dark. This overlap of the gaseous CO_2 presence and the accelerated formation of CO suggests that light-induced CO rate is connected to a reaction channel that does not occur through the formate or carbonate intermediates. The gaseous CO is observed much longer after gas phase CO_2 is removed, suggesting the slow decomposition of most abundant surface species into CO, as well as desorption of CO from the metallic Cu sites, as evidenced through the attenuation of the characteristic carbonyl bands on metallic copper, located at 2060 cm^{-1}, Fig. 5C and D [42]. We analyzed the effect of light on the CO desorption dynamics from the CZA catalyst, which could, be due to different CO adsorption strength under illumination, (Fig. S7B). The transient response curves of CO decay in the presence of the CZA under dark and illuminated conditions during the switch overlap entirely, which suggests equal interaction and holdup of CO on the CZA catalyst.

Based on the transient response data during *in-situ* DRIFTS experiment shown in Figs. 5 and S7, redox mechanism analysis in Fig. S5 and accompanying Supplementary note, CO appears to be formed marginally through the redox mechanism (about 10 % overall), partly through hydrogenation and decomposition of surface formates and carbonates, and during illumination mainly through the spectroscopically elusive carboxylate mechanism, which will be indirectly probed below.

We further quantitatively analyzed the possibility of copper oxidation state variation with *in-situ* XRD (Fig. S8E and Table S3) after dark and illuminated CZA activation (in 5 % H_2/Ar flow), as well as under RWGS conditions (in 50 % H_2/50 % CO_2 flow). This analysis was inspired by the possible transfer of radiative energy from the plasmon Cu states to the CuO_x phase either *via* dipole-dipole interactions or direct LSPR-mediated transient electron injection, resulting in weakening of the Cu—O chemical bonds and leading to altered Cu and CuO ratios during dark and light-assisted RWGS reaction.

Only metallic copper and ZnO crystalline phases could be identified in the CZA catalyst after activation and during the RWGS reaction. The

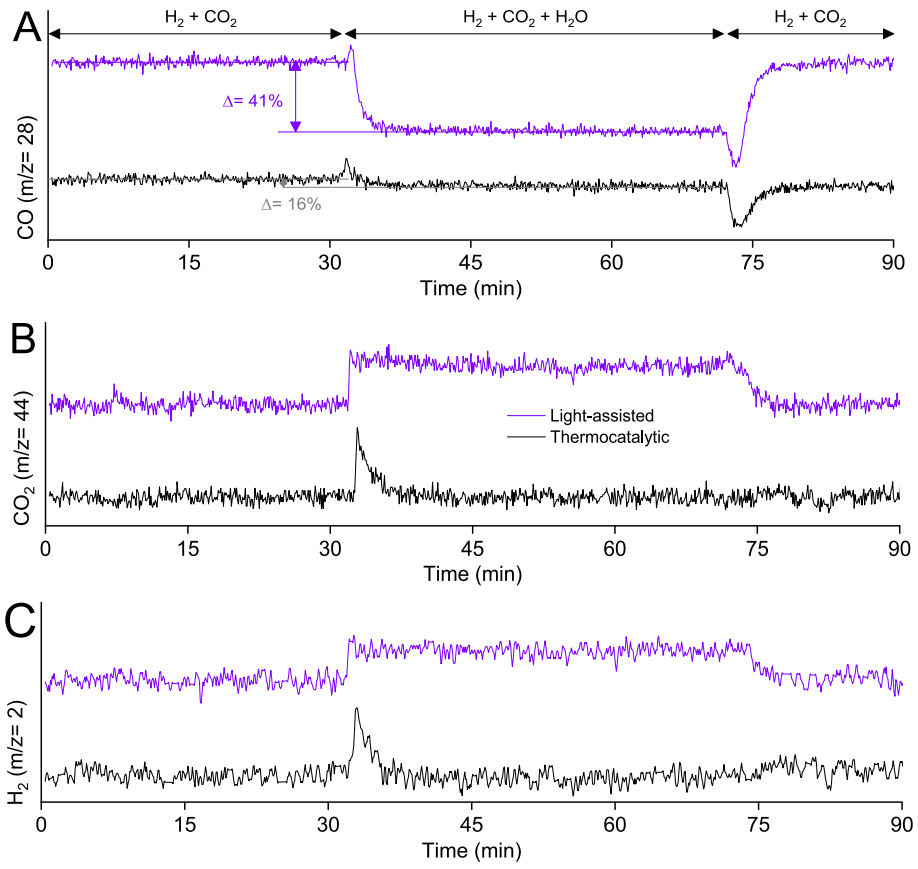

Fig. 6. Transient behavior of the CZA catalyst during step-change experiments between dry (3 %H_2/3 %CO_2/Ar) wet (3 %H_2/3 %CO_2/1 %H_2O/Ar) and back to dry (3 %H_2/3 %CO_2/Ar) feed at 230 °C. A) CO signal, B) CO_2 signal and C) H_2 signal. Catalyst illumination with 790 mW/cm^2 of white light was used during light-assisted experiment.

crystal size remained practically unchanged at about 10.3–11.9 and 7.7–8.3 nm for Cu and ZnO, respectfully, Table S3. According to the chemical composition of the CZA catalyst (see experimental section), the theoretical Cu/ZnO weight ratio is 1.4. This value assumes that all copper is reduced and crystalline, and that all ZnO remains in oxide form and is crystalline. The Cu/ZnO ratio in the activated catalyst increased slightly from 2.9 to 3.3 when activation under illumination was performed, which is in line with the theoretical calculations and experimental observation of light-promoted copper reduction [41,43]. The Cu/ZnO weight ratios during the dark and light-assisted RWGS reaction (Table S3) were slightly higher (3.6) compared to the values after catalyst activation. This is likely a consequence of a higher H_2 concentration during the reaction compared to activation (50 and 5 %, respectively). From the Cu/ZnO ratio of 3.6 we can calculate that around 50 % of ZnO is present as metallic Zn phase closely interacting with copper and forming a CuZn brass phase [17,44–46]. It was not possible to distinguish between the CuZn and Cu diffractions since they overlap closely and the peak shape is broad. Based on the absence of light-induced structural (crystal size) and oxidation state changes (Cu/ZnO ratio) during the RWGS under dark and light assisted conditions, we postulate that the CO rate acceleration originates from an electronic effect of CZA photoexcitation.

Our experiments confirmed that CO forming *via* the redox pathway at 230 °C (Fig. S5) is increased during illumination by 35 %, yet contributes only about 10 % to the total CO amount. The improvement is likely related to higher degree of catalyst reduction, as quantified during *in-situ* XRD analysis (Fig. S8E and Table S3). As a result, more redox capable Cu or CuZn brass sites can contribute to direct CO_2 reduction during illumination of the CZA. Also, there is no increase in formate and limited increase in carbonate reactivity at 230 °C (Table 1) that could contribute to the 346 % higher CO rate measured under illumination at 230 °C (Fig. 4A). Since the redox and formate reaction channels together cannot explain the experimentally measured CO rate acceleration under illumination, we postulate that the elusive, third reaction channel that is determining the CO formation is likely related to minority species like carboxylate. The carboxyl intermediate, which is widely regarded as the main RWGS channel, has very low surface coverage, as estimated *via* microkinetic modelling, implying that COOH is a very reactive intermediate, making it very difficult to identify directly spectroscopically or experimentally [28,39,40]. Water plays a crucial role in enabling the carboxylate mechanism [47]. Mavrikakis and colleagues used DFT and analyzed two pathways for carboxylate formation on Cu [111]: CO_2* + H* → COOH* + *, ($\Delta E = 0.39$ eV, $E_a = 1.8$ eV). The second pathway is energetically much more favorable and thus more likely to occur: CO_2* + H_2O* → COOH* + OH* ($\Delta E = 0.4$ eV, Ea = 0.82 eV).

Dissociation of carboxylate (COOH* + * → CO* + OH*) has an activation barrier of 0.59 eV and is thermo neutral, $\Delta E = -0.02$ eV [40]. Atomic hydrogen species are required to react with surface hydroxyls and form water, which will after desorption close the catalytic cycle and vacate the active site for the subsequent catalytic cycle. Atomic H can come from H_2 dissociation which is exothermic by 0.5 eV and is associated with an energy barrier of 0.53 eV. Water dissociation (H_2O* + * → OH* + H*) has an energy barrier of 1.36 eV and is rate limiting in WGS reaction over copper (111) surface [40].

Based on the crucial role of water for enabling the energetically favorable carboxylate genesis and being involved in the cleaning the catalytic surface *via* water desorption after carboxylate dehydroxylation (H* + OH* → 2* + H_2O), we analyzed its effect on the RWGS activity (and indirectly on the carboxylate pathway) by employing step-change experiments under dark and illuminated conditions, Fig. 6.

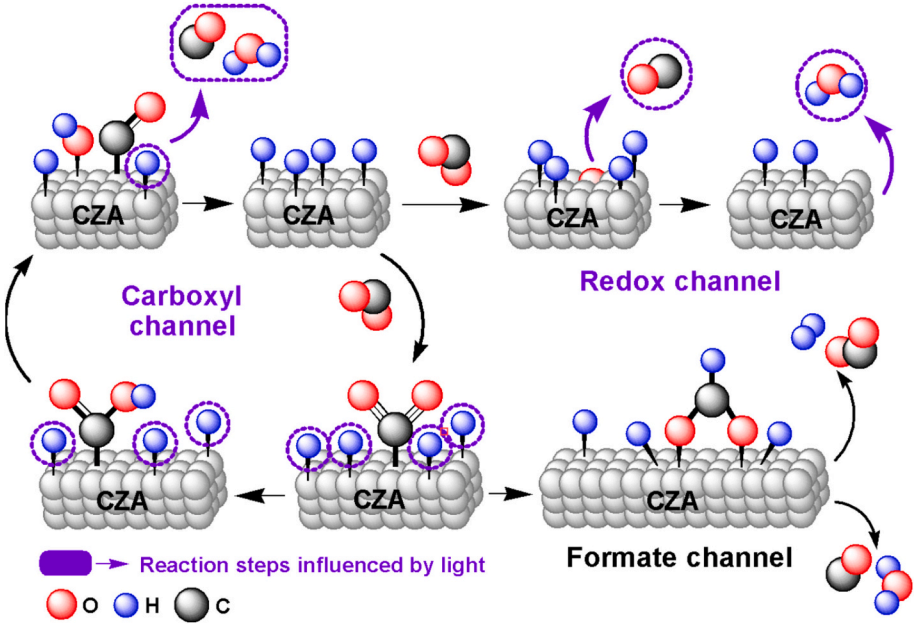

Fig. 7. Proposed RWGS reaction pathways over the CZA catalyst.

Dark RWGS: After reaching steady-state RWGS activity in a dry 3 % H_2/3 %CO_2/Ar flow, a switch to wet 3 %H_2/3 %CO_2/1 %H_2O/Ar flow (t ≈ 33 min) was made, black trace in Fig. 6A. The CO signal dropped by 16 %, revealing lower catalytic activity in the presence of co-fed water. Immediately after the switch, CO, CO_2 and H_2 signals rapidly increased in a pulse-like manner before returning to new steady-state values (Fig. 6A–C, t ≈ 33 min). Such response is likely related to water causing desorption of CO and carbonates, as well as formate decomposition *via* dehydrogenation and dehydroxylation channels: HCOO* + H* → CO_2 + H_2 and HCOO* + H* → CO + H_2O. Our previous work on Cu/Al_2O_3 catalyst identified higher reactivity of formate under dark RWGS conditions and its preferential dehydrogenation into CO_2 and H_2, which is in line with the behavior observed here over CZA [21].

Also, if COOH formation was the RDS and COOH formation was accelerated by higher water concentration through an energetically most favorable pathway identified theoretically [47], the CO rate should increase. As this was not the case, we postulate that carboxylate decomposition (*COOH + * → CO* + OH*) and more importantly, water formation and desorption (OH* + H* → H_2O + 2*) are the rate determining steps in dark RWGS. Adding water apparently shifts the water forming reaction towards water dissociation into OH and H, thus negatively impacting the RDS. After the 3 %H_2/3 %CO_2/1 %H_2O/Ar → 3 %H_2/3 %CO_2/Ar switch back to dry RWGS conditions (t ≈ 73 min), the CO signal dip (t ≈ 73 min) reveals the establishment of a new steady-state surface population with CO, which is higher under the dry conditions.

Light-assisted RWGS: Switching from a dry 3 %H_2/3 %CO_2/Ar to a wet 3 %H_2/3 %CO_2/1 %H_2O/Ar flow (t ≈ 33 min) caused the CO signal to drop by 41 %, revealing a much stronger and negative effect of water on the light-assisted reaction pathway compared to dark RWGS, Fig. 6A. With water co-feeding, we increase its surface population, thus negatively influence the COOH decomposition and associated water desorption. The step-wise drop of CO signal was accompanied by a step-wise increase of CO_2 and H_2 signals (Fig. 6B and C), resulting from their higher concentration (lower conversion) during water presence. Based on the absence of the pulse-like CO_2 and H_2 features at the time of the switch, there appears to be virtually no H_2 or carbonate displacement by water taking place. This observation can be rationalized by considering stronger H binding, evaluated from H_2-TPD experiment, and much more stable polydentate carbonate on the illuminated CZA (Table 1).

After the 3 %H_2/3 %CO_2/1 %H_2O/Ar → 3 %H_2/3 %CO_2/Ar switch back to dry RWGS conditions (t ≈ 73 min), the initial RWGS activity under illuminated conditions was restored, revealing the reversible effect of water. The CO signal dip during the switch is a consequence of establishment of steady-state surface population with CO, which is again higher under the dry conditions.

We must emphasize also that water influence on the redox and formate/carbonate reaction channels cannot be ignored, nor exactly quantified. However, the main influenced reaction channel by water is assumed to be the carboxylate pathway, based on the following rationale. The extent of CZA activity loss in wet RWGS feed is 2.5 times higher during illumination (41 and 16 %, respectively), as calculated from the drop of the CO signal values in Fig. 6A. We further suggest that the light-induced CO rate increase (2.9-fold, again calculated based on the increase of the CO signal form Fig. 6A) occurs exclusively at the account of accelerated carboxylate pathway. This assumption is based on the evidence that light-assisted redox reaction contribution remains marginal at 10 % and the reactivity of surface bidentate carbonate and formate remain unchanged, L/T ratios in Table 1. Under light-assisted conditions, the contribution of the redox reaction pathway to the CO yield is 11 % (Fig. S5), yet the water induced activity drop was 41 %. In this case, the water effect extends far beyond that of full inhibition of the redox mechanism and other reaction channels are affected. We further postulate that the formate dehydration reaction that yields CO (HCOO* + H* → H_2O + CO) could be thermodynamically shifted to the left because of water presence. As a result, water induced inhibition of the formate dehydration reaction cannot be excluded.

Based on the results of kinetic analysis, H_2-TPD, *in-situ* DRIFTS analysis, redox mechanism probing and transient isothermal water effect probing, we propose the following interconnectivity of reaction pathways during the light-assisted RWGS reaction over CZA, Fig. 7.

4. Conclusion

The CO formation rate can be accelerated almost 6-times with 790 mW/cm^2 of visible-light illumination on the CZA catalyst. The benefit of light is maximized at temperatures below 230 °C, which makes the light-assisted RWGS reaction a powerful, low-temperature CO_2 valorization opportunity. The observed acceleration of the CO rate upon illumination is accompanied by a notable decrease of Ea values from 83 to 44 kJ/mol

and a decrease of the H_2 reaction order from 0.81 to −2.6, while the CO_2 reaction order remains mostly unchanged. The most efficient light-driven activation of the catalyst is *via* excitation of the inter band transitions of copper with photons in the 400–500 nm range, which resulted in the AQY values of up to 47 %. Redox mechanism is operational under both dark and illuminated conditions, but in both cases contributes only about 10 % to the CO productivity. Transient experiments using *in-situ* DRIFT spectroscopy revealed that reactivity of most abundant surface species (formates and carbonates) is not improved under illumination, meaning that they do not represent kinetically relevant reaction intermediates for CO generation under illuminated reaction conditions. CO is thus likely formed through the carboxylate intermediate. Under illumination, H_2 dissociation and surface coverage with H* is enhanced about 5-fold compared to dark conditions. As a result, the dissociation of carboxylate ($COOH^* + * \rightarrow CO^* + HO^*$) is accelerated through high H* coverage helping with $H^* + OH^*$ recombination and water desorption, which is the underlying mechanistic reason for light-assisted CO rate acceleration.

CRediT authorship contribution statement

Miha Okorn: Writing – original draft, Investigation, Formal analysis. **Giovanni Cardolini Rizzo:** Investigation, Formal analysis, Data curation. **Kristijan Lorber:** Writing – review & editing, Visualization, Methodology, Investigation. **Matjaž Mazaj:** Writing – review & editing, Investigation, Formal analysis. **Nataša Novak Tušar:** Writing – review & editing, Resources, Project administration. **Petar Djinović:** Writing – review & editing, Supervision, Resources, Project administration, Funding acquisition, Conceptualization.

Declaration of competing interest

The authors declare the following financial interests/personal relationships which may be considered as potential competing interests: Petar Djinovic reports financial support was provided by Slovenian Research and Innovation Agency. If there are other authors, they declare that they have no known competing financial interests or personal relationships that could have appeared to influence the work reported in this paper.

Acknowledgements

Slovenian Research and Innovation Agency (ARIS) funded this research through grants P1-0418 and N2-0265. Mojca Opresnik, Dr. Janvit Teržan and Edi Kranjc are kindly acknowledged for their assistance with SEM-EDX and XRD analyses.

Appendix A. Supplementary data

Supplementary data to this article can be found online at https://doi.org/10.1016/j.cej.2025.171682.

Data availability

Data will be made available on request.

References

[1] E. Schwab, A. Milanov, S.A. Schunk, A. Behrens, N. Schödel, Dry reforming and reverse water gas shift: alternatives for syngas production? Chem. Ing. Tech. 87 (2015) 347–353, https://doi.org/10.1002/cite.201400111.
[2] D. Vovchok, C. Zhang, S. Hwang, L. Jiao, F. Zhang, Z. Liu, S.D. Senanayake, J. A. Rodriguez, Deciphering dynamic structural and mechanistic complexity in Cu/CeO_2/ZSM-5 catalysts for the reverse water-gas shift reaction, ACS Catal. 10 (2020) 10216–10228, https://doi.org/10.1021/acscatal.0c01584.
[3] K. Lorber, P. Djinović, Accelerating photo-thermal CO_2 reduction to CO, CH_4 or methanol over metal/oxide semiconductor catalysts, IScience 25 (2022) 104107, https://doi.org/10.1016/j.isci.2022.104107.
[4] Z. Wang, H. Song, H. Liu, J. Ye, Coupling of solar energy and thermal energy for carbon dioxide reduction status and prospects, Angew. Chem. 132 (2020) 8092–8111, https://doi.org/10.1002/ange.201907443.
[5] X. Li, J. Yu, M. Jaroniec, X. Chen, Cocatalysts for selective photoreduction of CO_2 into solar fuels, Chem. Rev. 119 (2019) 3962–4179, https://doi.org/10.1021/acs.chemrev.8b00400.
[6] P. Djinović, J. Batista, A. Pintar, Calcination temperature and CuO loading dependence on CuO-CeO_2 catalyst activity for water-gas shift reaction, Appl. Catal. A Gen. 347 (2008) 23–33, https://doi.org/10.1016/j.apcata.2008.05.027.
[7] Y. Choi, G.D. Sim, U. Jung, Y. Park, M.H. Youn, D.H. Chun, G.B. Rhim, K.Y. Kim, K. Y. Koo, Copper catalysts for CO_2 hydrogenation to CO through reverse water–gas shift reaction for e-fuel production: fundamentals, recent advances, and prospects, Chem. Eng. J. 492 (2024) 152283, https://doi.org/10.1016/j.cej.2024.152283.
[8] A.M. Bahmanpour, M. Signorile, O. Kröcher, Recent progress in syngas production via catalytic CO_2 hydrogenation reaction, Appl. Catal. B 295 (2021) 120319, https://doi.org/10.1016/j.apcatb.2021.120319.
[9] W.D. Williams, J.P. Greeley, W.N. Delgass, F.H. Ribeiro, Water activation and carbon monoxide coverage effects on maximum rates for low temperature water-gas shift catalysis, J. Catal. 347 (2017) 197–204, https://doi.org/10.1016/j.jcat.2017.01.016.
[10] X. Su, X. Yang, B. Zhao, Y. Huang, Designing of highly selective and high-temperature endurable RWGS heterogeneous catalysts: recent advances and the future directions, J. Energy Chem. 26 (2017) 854–867, https://doi.org/10.1016/j.jechem.2017.07.006.
[11] Z. Yang, M. Zeng, K. Wang, X. Yue, X. Chen, W. Dai, X. Fu, Visible light-assisted thermal catalytic reverse water gas reaction over Cu-CeO_2: the synergistic of hot electrons and oxygen vacancies induced by LSPR effect, Fuel 315 (2022) 123186, https://doi.org/10.1016/j.fuel.2022.123186.
[12] B. Xie, R.J. Wong, T.H. Tan, M. Higham, E.K. Gibson, D. Decarolis, J. Callison, K. F. Aguey-Zinsou, M. Bowker, C.R.A. Catlow, J. Scott, R. Amal, Synergistic ultraviolet and visible light photo-activation enables intensified low-temperature methanol synthesis over copper/zinc oxide/alumina, Nat. Commun. 11 (2020), https://doi.org/10.1038/s41467-020-15445-z.
[13] Z. Zhu, J. Zhou, Q. Li, Z. Liu, Q. Deng, Z. Zhou, C. Li, L. Fu, J. Zhou, H. Li, Q. Zhang, K. Wu, Preparation of heterostructured Cu-CeO_2/$SrTiO_3$ catalysts by rapid plasma exsolution for photothermal reverse water gas shift reaction, J. CO_2 Util. 80 (2024) 102665, https://doi.org/10.1016/j.jcou.2023.102665.
[14] K. Lorber, J. Zavašnik, J. Sancho-Parramon, M. Bubaš, M. Mazaj, P. Djinović, On the mechanism of visible-light accelerated methane dry reforming reaction over Ni/CeO_{2-x} catalysts, Appl. Catal. B 301 (2022) 120745, https://doi.org/10.1016/j.apcatb.2021.120745.
[15] S.D. Jones, L.M. Neal, H.E. Hagelin-Weaver, Steam reforming of methanol using Cu-ZnO catalysts supported on nanoparticle alumina, Appl. Catal. B 84 (2008) 631–642, https://doi.org/10.1016/j.apcatb.2008.05.023.
[16] M. Zabilskiy, V.L. Sushkevich, D. Palagin, M.A. Newton, F. Krumeich, J.A. van Bokhoven, The unique interplay between copper and zinc during catalytic carbon dioxide hydrogenation to methanol, Nat. Commun. 11 (2020) 2409, https://doi.org/10.1038/s41467-020-16342-1.
[17] A. Beck, M. Zabilskiy, M.A. Newton, O. Safonova, M.G. Willinger, J.A. van Bokhoven, Following the structure of copper-zinc-alumina across the pressure gap in carbon dioxide hydrogenation, Nat. Catal. 4 (2021) 488–497, https://doi.org/10.1038/s41929-021-00625-x.
[18] C. Lee, Y. Park, J.Y. Park, Hot electrons generated by intraband and interband transition detected using a plasmonic Cu/TiO_2 nanodiode, RSC Adv. 9 (2019) 18371–18376, https://doi.org/10.1039/c9ra02601k.
[19] P. Liu, H. Wang, X. Li, M. Rui, H. Zeng, Localized surface plasmon resonance of Cu nanoparticles by laser ablation in liquid media, RSC Adv. 5 (2015) 79738–79745, https://doi.org/10.1039/c5ra14933a.
[20] C. Wei, Q. Liu, Shape-, size-, and density-tunable synthesis and optical properties of copper nanoparticles, CrystEngComm 19 (2017) 3254–3262, https://doi.org/10.1039/c7ce00750g.
[21] K. Lorber, I. Arčon, M. Huš, J. Zavašnik, J. Sancho-Parramon, A. Prašnikar, B. Likozar, N. Novak Tušar, P. Djinović, Light-assisted catalysis and the dynamic nature of surface species in the reverse water gas shift reaction over Cu/γ-Al_2O_3, ACS Appl. Mater. Interfaces 16 (2024) 67778–67790, https://doi.org/10.1021/acsami.4c15849.
[22] J. Schumann, M. Eichelbaum, T. Lunkenbein, N. Thomas, M.C. Álvarez Galván, R. Schlögl, M. Behrens, Promoting strong metal support interaction: doping ZnO for enhanced activity of Cu/ZnO:M (M = Al, Ga, Mg) catalysts, ACS Catal. 5 (2015) 3260–3270, https://doi.org/10.1021/acscatal.5b00188.
[23] K.-H. Ernst, C.T. Campbell, G. Moretti, Kinetics of the reverse water-gas shift reaction over Cu(110), J. Catal. 134 (1992) 66–74, https://doi.org/10.1016/0021-9517(92)90210-9.
[24] A.A. Upadhye, I. Ro, X. Zeng, H.J. Kim, I. Tejedor, M.A. Anderson, J.A. Dumesic, G. W. Huber, Plasmon-enhanced reverse water gas shift reaction over oxide supported Au catalysts, Catal. Sci. Technol. 5 (2015) 2590–2601, https://doi.org/10.1039/c4cy01183j.
[25] X. Zhang, X. Li, M.E. Reish, D. Zhang, N.Q. Su, Y. Gutiérrez, F. Moreno, W. Yang, H. O. Everitt, J. Liu, Plasmon-enhanced catalysis: distinguishing thermal and nonthermal effects, Nano Lett. 18 (2018) 1714–1723, https://doi.org/10.1021/acs.nanolett.7b04776.
[26] D. Mateo, J.L. Cerrillo, S. Durini, J. Gascon, Fundamentals and applications of photo-thermal catalysis, Chem. Soc. Rev. 50 (2021) 2173–2210, https://doi.org/10.1039/d0cs00357c.

[27] M.J. Kale, T. Avanesian, P. Christopher, Direct photocatalysis by plasmonic nanostructures, ACS Catal. 4 (2014) 116–128, https://doi.org/10.1021/cs400993w.
[28] N.C. Nelson, M.T. Nguyen, V.A. Glezakou, R. Rousseau, J. Szanyi, Carboxyl intermediate formation via an in situ-generated metastable active site during water-gas shift catalysis, Nat. Catal. 2 (2019) 916–924, https://doi.org/10.1038/s41929-019-0343-2.
[29] C. Chen, W. Cheng, S. Lin, Mechanism of CO formation in reverse water-gas shift reaction over Cu/Al2O3 catalyst, Catal. Lett. 68 (2000) 45–48, https://doi.org/10.1023/A:1019071117449.
[30] E.L. Kunkes, F. Studt, F. Abild-Pedersen, R. Schlögl, M. Behrens, Hydrogenation of CO_2 to methanol and CO on $Cu/ZnO/Al_2O_3$: is there a common intermediate or not? J. Catal. 328 (2015) 43–48, https://doi.org/10.1016/j.jcat.2014.12.016.
[31] X. Wang, H. Shi, J.H. Kwak, J. Szanyi, Mechanism of CO_2 hydrogenation on Pd/Al_2O_3 catalysts: kinetics and transient DRIFTS-MS studies, ACS Catal. 5 (2015) 6337–6349, https://doi.org/10.1021/acscatal.5b01464.
[32] A. Goguet, F.C. Meunier, D. Tibiletti, J.P. Breen, R. Burch, Spectrokinetic investigation of reverse water-gas-shift reaction intermediates over a Pt/CeO_2 catalyst, J. Phys. Chem. B 108 (2004) 20240–20246, https://doi.org/10.1021/jp047242w.
[33] M.J.L. Ginés, A.J. Marchi, C.R. Apesteguía, Kinetic study of the reverse water-gas shift reaction over $CuO/ZnO/Al_2O_3$ catalysts, Appl. Catal. A Gen. 154 (1997) 155–171, https://doi.org/10.1016/S0926-860X(96)00369-9.
[34] K. Lorber, J. Zavašnik, I. Arčon, M. Huš, J. Teržan, B. Likozar, P. Djinović, CO_2 activation over nanoshaped CeO_2 decorated with nickel for low-temperature methane dry reforming, ACS Appl. Mater. Interfaces 14 (2022) 31862–31878, https://doi.org/10.1021/acsami.2c05221.
[35] J. Szanyi, J.H. Kwak, Dissecting the steps of CO_2 reduction: 1. The interaction of CO and CO_2 with γ-Al_2O_3: an in situ FTIR study, Phys. Chem. Chem. Phys. 16 (2014) 15117–15125, https://doi.org/10.1039/C4CP00616J.
[36] K. Lorber, V. Shvalya, J. Zavašnik, D. Vengust, I. Arčon, M. Huš, A. Pavlišič, J. Teržan, U. Cvelbar, B. Likozar, P. Djinović, Non-oxidative calcination enhances the methane dry reforming performance of Ni/CeO_{2-x} catalysts under thermal and photo-thermal conditions, J. Mater. Chem. A 12 (2024) 19910–19923, https://doi.org/10.1039/D4TA01823K.
[37] B. Smith, Infrared Spectral Interpretation, CRC Press, 2018, https://doi.org/10.1201/9780203750841.
[38] C. Ledesma, J. Yang, D. Chen, A. Holmen, Recent approaches in mechanistic and kinetic studies of catalytic reactions using SSITKA technique, ACS Catal. 4 (2014) 4527–4547, https://doi.org/10.1021/cs501264f.
[39] Z. Zhang, S.-S. Wang, R. Song, T. Cao, L. Luo, X. Chen, Y. Gao, J. Lu, W.-X. Li, W. Huang, The most active Cu facet for low-temperature water gas shift reaction, Nat. Commun. 8 (2017) 488, https://doi.org/10.1038/s41467-017-00620-6.
[40] A.A. Gokhale, J.A. Dumesic, M. Mavrikakis, On the mechanism of low-temperature water gas shift reaction on copper, J. Am. Chem. Soc. 130 (2008) 1402–1414, https://doi.org/10.1021/ja0768237.
[41] J. Garcia-Prieto, M.E. Ruiz, O. Novaro, Role of excited atomic states in the active sites of transition metals for oxidative and reductive catalytic processes, J. Am. Chem. Soc. 107 (1985) 5635–5644, https://doi.org/10.1021/ja00306a008.
[42] M. Zabilskiy, P. Djinović, B. Erjavec, G. Dražić, A. Pintar, Small CuO clusters on CeO_2 nanospheres as active species for catalytic N_2O decomposition, Appl. Catal. B 163 (2015) 113–122, https://doi.org/10.1016/j.apcatb.2014.07.057.
[43] A. Marimuthu, J. Zhang, S. Linic, Tuning selectivity in propylene epoxidation by plasmon mediated photo-switching of Cu oxidation state, Science 339 (1979) (2013) 1590–1593, https://doi.org/10.1126/science.1231631.
[44] S. Saedy, M.A. Newton, M. Zabilskiy, J.H. Lee, F. Krumeich, M. Ranocchiari, J. A. van Bokhoven, Copper–zinc oxide interface as a methanol-selective structure in Cu–ZnO catalyst during catalytic hydrogenation of carbon dioxide to methanol, Catal. Sci. Technol. 12 (2022) 2703–2716, https://doi.org/10.1039/D2CY00224H.
[45] M. Behrens, F. Studt, I. Kasatkin, S. Kühl, M. Hävecker, F. Abild-Pedersen, S. Zander, F. Girgsdies, P. Kurr, B.-L. Kniep, M. Tovar, R.W. Fischer, J.K. Nørskov, R. Schlögl, The active site of methanol synthesis over $Cu/ZnO/Al_2O_3$ industrial catalysts, Science 336 (2012) 893–897, https://doi.org/10.1126/science.1219831.
[46] A. Beck, M.A. Newton, M. Zabilskiy, P. Rzepka, M.G. Willinger, J.A. van Bokhoven, Drastic events and gradual change define the structure of an active copper-zinc-alumina catalyst for methanol synthesis, Angew. Chem. Int. Ed. 61 (2022) e202200301, https://doi.org/10.1002/anie.202200301.
[47] Z. Li, N. Li, N. Wang, B. Zhou, P. Yin, B. Song, J. Yu, Y. Yang, Mechanism investigations on water gas shift reaction over Cu(111), Cu(100), and Cu(211) surfaces, ACS Omega 7 (2022) 3514–3521, https://doi.org/10.1021/acsomega.1c05991.